



Anion control as a strategy to achieve high-mobility and high-stability oxide thin-film transistors

SUBJECT AREAS:
ELECTRONIC PROPERTIES
AND MATERIALS
SEMICONDUCTORS
ELECTRONIC DEVICES
ELECTRONIC STRUCTURE

Hyun-Suk Kim^{1*}, Sang Ho Jeon^{2*}, Joon Seok Park¹, Tae Sang Kim¹, Kyoung Seok Son¹, Jong-Baek Seon¹, Seok-Jun Seo¹, Sun-Jae Kim¹, Eunha Lee³, Jae Gwan Chung³, Hyungik Lee³, Seungwu Han², Myungkwan Ryu¹, Sang Yoon Lee¹ & Kinam Kim¹

Received
24 October 2012

Accepted
20 February 2013

Published
15 March 2013

Correspondence and requests for materials should be addressed to S.H. (hansw@snu.ac.kr); M.R. (myungkwan.ryu@samsung.com) or S.Y.L. (sangyoon.lee@samsung.com)

* These authors contributed equally to this work.

¹Display Device Laboratory, Samsung Advanced Institute of Technology, Samsung Electronics Corporation, Yongin-Si, Gyeonggi-Do 446-712, Republic of Korea, ²Department of Materials Science and Engineering and Research Institute of Advanced Materials, Seoul National University, Seoul 151-744, Republic of Korea, ³Analytical Science Group, Samsung Advanced Institute of Technology, Samsung Electronics Corporation, Yongin-Si, Gyeonggi-Do 446-712, Republic of Korea.

Ultra-definition, large-area displays with three-dimensional visual effects represent megatrend in the current/future display industry. On the hardware level, such a “dream” display requires faster pixel switching and higher driving current, which in turn necessitate thin-film transistors (TFTs) with high mobility. Amorphous oxide semiconductors (AOS) such as In-Ga-Zn-O are poised to enable such TFTs, but the trade-off between device performance and stability under illumination critically limits their usability, which is related to the hampered electron-hole recombination caused by the oxygen vacancies. Here we have improved the illumination stability by substituting oxygen with nitrogen in ZnO, which may deactivate oxygen vacancies by raising valence bands above the defect levels. Indeed, the stability under illumination and electrical bias is superior to that of previous AOS-based TFTs. By achieving both mobility and stability, it is highly expected that the present ZnON TFTs will be extensively deployed in next-generation flat-panel displays.

The introduction of flat-panel, thin-film transistor liquid-crystal display (TFT-LCD) enormously expanded the horizon of display application by enabling production of large-screen TV sets and various mobile devices. Nevertheless, the demand for more realistic visual experiences is driving academic as well as industrial research efforts towards next-generation displays incorporating “ultra” definition (4000 × 2000 pixels), large-area (> 70 inch), and three-dimensional effects. The feasibility of such high-end devices, whether employing liquid crystal or organic light-emitting diode (OLED), hinges on high performance TFT components that can switch on or off each pixel at unprecedented rates. Technically, a transistor that exhibits field-effect mobility values higher than 20 cm²V⁻¹s⁻¹ is required^{1,2}.

Most of present LCD devices employ hydrogenated amorphous silicon (a-Si:H) as the channel layer in TFTs owing to low fabrication cost and excellent cell-to-cell uniformity. However, the directional *sp*³ bonding intrinsically limits the field-effect mobility of amorphous silicon below 1 cm²V⁻¹s⁻¹, which is far lower than the above requisite for next-generation displays. Nomura *et al.* demonstrated that the intrinsic drawback of the amorphous network can be circumvented by employing materials with non-directional *s* character in the conduction band such as In-Ga-Zn-O (a-IGZO), so called amorphous oxide semiconductors (AOS)^{3,4}. Several prototypical displays incorporating AOS-TFTs have been demonstrated with promising results^{2,5}.

However, it is suggested that the presence of donor-like oxygen vacancies (Vo) located within the wide bandgap of AOS (ref. 6), which is also critical for the high mobility^{7,8}, leads to slow decay of photogenerated current when light and negative gate bias are applied, and hence significantly compromises device stability by shifting the threshold voltage^{9–11}. This negative-bias illumination (NBI) instability makes AOS remain conductive for several hours/days, even in the absence of light. Therefore, such slow recovery also limits the switching speed of TFTs and the frame rates in flat-panel displays (FPDs)¹². Although the approaches to resolve the NBI instability by applying short positive gate pulses inducing electron accumulation and accelerating the recombination with ionized Vo sites have been recently reported, they can only be applied to three-terminal devices along with the complex bias scheme^{12,13}. Therefore, a more fundamental solution, which could be adapted to a variety of oxide systems and device architectures, is in high demand.



In this work, through the careful consideration of the electronic band structure of the most well-known oxide semiconductor ZnO, where problematic V_o levels are located near its valence band maximum (VBM), we have hypothesized that the NBI instability could be suppressed via the control over the valence band by the substitution of non-oxide anions for the oxygen anions that contribute to the top portion of valence band. Therefore, it is believed that the larger size anions (N^{3-} , S^{2-} , Se^{2-} and so on; refs 14–18) with higher p orbital energy than oxygen may deactivate or remove oxygen vacancies by increasing the valence band energy, as shown in Fig. 1a.

Here, we present a combined experimental and theoretical study on Zn_3N_2 -alloyed ZnO (or ZnON) to elucidate the possibility of tuning the valence band to deactivate the deep V_o level in oxide semiconductors. Through the substitutional alloying with nitrogen anions, we successfully increase the VBM by as high as ~ 1.6 eV compared to pure ZnO, which is sufficiently higher than the theoretically reported V_o levels (located within 1 eV above VBM; ref. 19) in the ZnO bandgap. To verify our strategy, we fabricated and electrically tested the TFTs that use amorphous-like ZnON films as the active channel layer. While having high field-effect mobility exceeding $30 \text{ cm}^2\text{V}^{-1}\text{s}^{-1}$, the TFTs based on ZnON exhibit little signature of the NBI instability and also excellent device stability

under illumination with visible light, compared to conventional AOS-devices with similar mobility values. As such, the device may rival a -Si:H TFTs that have been widely adopted in active-matrix LCDs in terms of long-term stability.

Results

Films of ZnON were prepared by reactive radio-frequency magnetron sputtering using a Zn target in oxygen and nitrogen atmosphere, which was developed by Ye *et al.* (ref. 20). In order to control anion contents within the film, oxygen partial pressure in the chamber was varied between 3.6–28.1 mPa during deposition. The composition of the grown sample was measured by Rutherford backscattering spectroscopy and the oxygen (nitrogen) content was found to increase (decrease) with the oxygen partial pressure, taking up below 5 to 40% of the total atoms while the Zn fraction was kept nearly constant at $\sim 55\%$ (see Supplementary Fig. S1a). All grown films were n-type semiconductors when characterized by Hall measurements. The carrier concentration significantly decreases from $\sim 3.0 \times 10^{18}$ to $\sim 2.0 \times 10^{16} \text{ cm}^{-3}$ as the oxygen partial pressure increases, indicating that oxygen may act as a carrier suppressor (Supplementary Fig. S1b). The Hall mobility increases as the carrier concentration increases, which might be understood by the percolation model similar to the

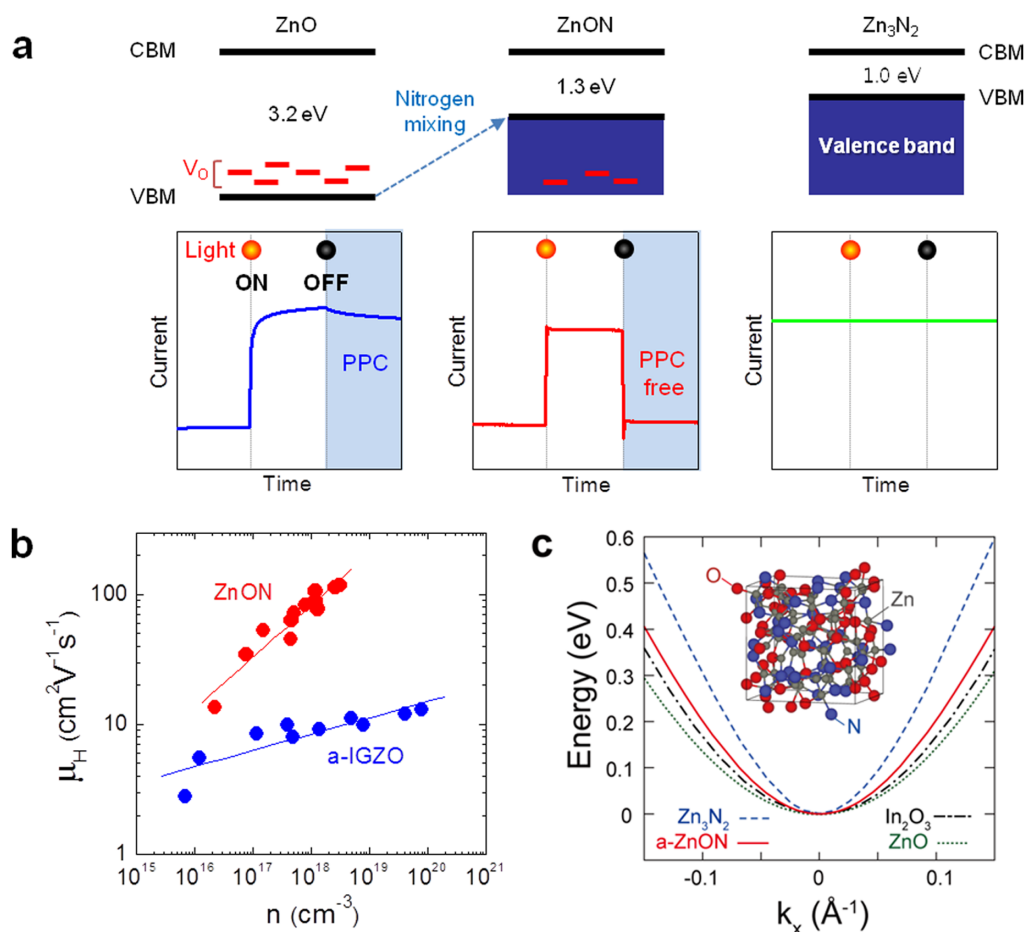


Figure 1 | Valence band control of oxide semiconductor to deactivate the oxygen vacancy, and high-mobility properties of amorphous-like ZnON. (a) Schematic band diagrams of ZnO (optical bandgap = 3.2 eV), ZnON (1.3 eV), and Zn₃N₂ (1.0 eV), and ZnON (1.3 eV). The persistent photocurrent (PPC) under negative gate bias, which is related to donor-like oxygen vacancies (V_o) located within the wide bandgap, is found in the typical oxide semiconductor ZnO. On the other hand, such an effect is not expected in ZnON, where the nitrogen anions with higher p orbital energy than oxygen may passivate or remove V_o by increasing the valence band maximum (VBM) energy level. Zn₃N₂ exhibits conductor-like characteristics, not semiconducting due to the large number of electron carriers ($> 10^{19} \text{ cm}^{-3}$; ref. 21). (b) Relationship between Hall mobility and carrier concentration for ZnON films. Data on a-IGZO films are shown for comparison (ref. 1). (c) Conduction bands of c-ZnO, c-In₂O₃, c-Zn₃N₂, and a-ZnON are plotted along k_x with the conduction band minimum (CBM) aligned at 0 eV. Inset: The model unit cell of a-ZnON containing 60 Zn, 24 O, and 24 N atoms obtained from the melt-quench simulations.



case of a-IGZO (ref. 1), and large Hall mobilities ($\geq 50 \text{ cm}^2\text{V}^{-1}\text{s}^{-1}$) were obtained at carrier concentrations $\geq 10^{17} \text{ cm}^{-3}$ (Fig. 1b). It is noted that the Hall mobility of ZnON increases with the carrier concentration more rapidly than for a-IGZO. This could be attributed to the relatively low potential barriers above the conduction band edge of ZnON that is merely composed of single Zn^{2+} ions, unlike the random distribution of multiple cations (In^{3+} , Zn^{2+} , and Ga^{3+}) in a-IGZO (ref. 20). For all subsequent experiments, the film made at 14 mPa was used as the film shows high Hall mobility values ($\sim 50 \text{ cm}^2\text{V}^{-1}\text{s}^{-1}$) and reasonably low carrier concentrations of $\sim 10^{17} \text{ cm}^{-3}$. The chemical composition of the film is $\text{Zn}:\text{N}:\text{O} = 56.3:21.7:22.0$ (in atomic percent).

From grazing incidence angle X-ray diffraction (GIAXRD; Supplementary Fig. S2a), the ZnON films are confirmed to retain the amorphous-like structure up to an annealing temperature of 350°C , which corresponds to the maximum process temperature (i.e., for the gate insulator growth before ZnON deposition) for our TFT fabrication. It is believed that amorphous-like phase of ZnON is promoted by the competition between reactions for the growth of cubic Zn_3N_2 and for growth of hexagonal ZnO in a reactive sputtering process²⁰. Further transmission electron microscopy (TEM) images reveal the presence of a small fraction of nanocrystallites randomly dispersed in the amorphous matrix (Supplementary Fig. S2b). The films have a smooth surface topography with no discernible grain boundaries and a small root mean square surface roughness of 0.7 nm (Supplementary Fig. S2c). The X-ray photoelectron spectroscopy (XPS) data in Supplementary Fig. S3 show the existence of N-Zn and O-Zn bonds, confirming the formation of an oxynitride compound^{21,22}. The additional small O 1s peak at 531.4 eV is attributed to OH^- impurities which may originate from unintentional moisture adsorption before ex-situ XPS analysis, as the feature is more pronounced in the O 1s spectra collected at the top surface prior to Ar sputtering.

The insets of Fig. 2a show photographs of ZnON and ZnO films on glass substrates. While ZnO is highly transparent, ZnON has a darker color due to the enhanced absorption of light in the visible wavelength range (photon energy, $h\nu = 1.65 \sim 3.18 \text{ eV}$). Indeed, the optical bandgap estimated from the Tauc model is $\sim 1.3 \text{ eV}$ for ZnON (Fig. 2a), which is drastically reduced from 3.2 eV of ZnO and is slightly larger than that ($\sim 1.0 \text{ eV}$) of Zn_3N_2 (ref. 22,23), suggesting that ZnON is a narrow band gap semiconductor. It is also noted that there is a large Urbach tail in ZnO, which suggests the presence of a large density of subgap defect states mostly originating from Vo (ref. 12). Figure 2b shows the XPS spectra of the bandgap region near the valence band maximum (VBM). The VBM energy level of the ZnON film shifts upward by $\sim 1.6 \text{ eV}$ relative to ZnO, which is similar to the optical bandgap difference ($\sim 1.9 \text{ eV}$).

To understand the electronic structure of amorphous-like ZnON in comparison with conventional oxide/nitride semiconductors, first-principles calculations based on density functional theory (DFT) were performed. Amorphous structures were obtained through melt-quench simulations. To prevent the formation of N_2 molecules during the melting stage, the structure was melted briefly at 2000 K. (See Methods section for the full computational details.) The inset of Fig. 1c shows atomic structures of an amorphous ZnON (a-ZnON) with stoichiometry of $\text{Zn}_{60}\text{O}_{24}\text{N}_{24}$. It is found that the local order around each atom is similar to those in crystalline ZnO (c-ZnO) or Zn_3N_2 (c- Zn_3N_2). In Fig. 1c, the conduction bands of c-ZnO, c- In_2O_3 , c- Zn_3N_2 , and a-ZnON are compared since electron conduction is dominant in these materials. For comparison, the conduction band minima were aligned among different materials. Even though the dominant scattering mechanism in AOS is not clarified yet, the effective mass at the conduction band bottom should be an important parameter in any mechanism. It was shown that the conduction bands of AOS can be well fitted to the dispersion relation of a massive Dirac particle in the form of $E = \varepsilon_0 + \sqrt{\varepsilon^2 + \gamma^2 k^2}$, with ε_0 , ε ,

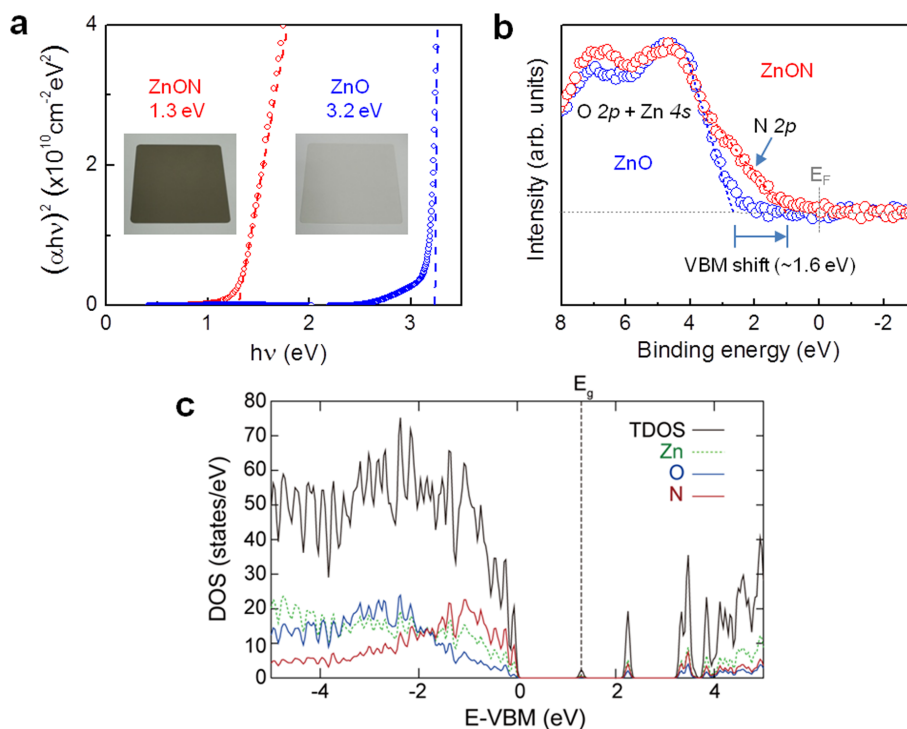


Figure 2 | Optical properties and electronic structures of ZnON. (a) Tauc plot; $(\alpha h\nu)^2$ as a function of photon energy $h\nu$, where ν is the photon frequency, indicating the optical bandgap (E_g) for ZnON (1.3 eV) and ZnO (3.2 eV) films. Insets: Photographs of ZnON and ZnO samples intuitively showing the effect of nitrogen incorporation on the bandgap reduction. (b) XPS spectra of the bandgap region for ZnO and ZnON films. The valence band offsets are determined by extrapolating the straight line regions of the onset spectra to the baseline. (c) Calculated total electronic DOS (TDOS) and projection onto the Zn, O, and N atoms for a-ZnON. The VBM energy level is set to 0 eV.



and γ as fitting parameters²⁴. The effective masses at Γ (m_e^*) inferred from this dispersion relation are 0.27, 0.22, 0.10, and 0.19 m_e for c-ZnO, c-In₂O₃, c-Zn₃N₂, and a-ZnON, respectively. Therefore, m_e^* of a-ZnON lies in between those of c-ZnO and c-Zn₃N₂, and is smaller than those of c-In₂O₃ and, presumably, AOS. Therefore, the high mobility of a-ZnON may originate from the smaller m_e^* .

Figure 2c shows the calculated total electronic density of states and their projection onto the Zn, O, and N atoms for a-ZnON. The bandgap reduction in a-ZnON is mainly due to N states (mostly N 2p character) in valence band, which is consistent with the experimental XPS data in Fig. 2b.

We fabricated more than 100 bottom-gate ZnON TFTs with Molybdenum (Mo) source-drain top contacts, which are the typical device structure of the AOS-TFTs (Fig. 3a). Figure 3b shows a cross-sectional TEM image of the fabricated ZnON TFT, where the gate, insulator, channel, etch stopper, and source/drain layers are well defined with excellent thickness uniformity, suggesting the absence of inter-diffusion between its constituent layers. The output and transfer characteristics were electrically measured and a typical example is illustrated in Fig. 3c and d. The source-to-drain current (I_{DS}) increases markedly with the source-to-drain voltage (V_{DS}) at a positive gate-to-source voltage (V_{GS}), indicating that the channel is indeed n-type (Fig. 3c). The I_{DS} - V_{DS} curve exhibits a clear pinch-off and current saturation without current-crowding in the low V_{DS} region, which suggests that the TFT operation is consistent with

the standard field-effect transistor theory²⁵. The transfer curve (Fig. 3d) shows that a low off-current of the order of 10^{-12} A, and an on-to-off current ratio $\sim 10^8$ are obtained. The threshold voltage (V_T) is positive (~ 5.4 V), suggesting that the TFT operates in enhancement mode. The gate leakage current (I_G) is orders of magnitude lower than the I_{DS} , which guarantees that the TFT characteristics are not affected by the gate leakage. The calculated saturation field-effect mobility (μ_{sat}) reaches a high value of $42.6 \text{ cm}^2\text{V}^{-1}\text{s}^{-1}$ which agrees roughly with the Hall mobility of ZnON films ($\sim 50 \text{ cm}^2\text{V}^{-1}\text{s}^{-1}$). However, a relatively large subthreshold swing (S) of ~ 1.2 V/decade and a hysteresis of ~ 0.7 V (Supplementary Fig. S4a) indicate that further improvements in the channel-insulator interface are in demand. In addition, it is speculated that the large S value of ZnON TFTs would have also originated from the generation of the tail states related to nitrogen vacancies with shallow defect states²⁶.

Next, we examine the photo-response against visible light illumination using a commercially available white-light LED (Fig. 3a). As references, conventional a-Si:H TFTs ($\mu_{sat} = 0.8 \text{ cm}^2\text{V}^{-1}\text{s}^{-1}$, $V_T = 3.2$ V, $S = 0.9$ V/decade) and a-IZO TFTs ($\mu_{sat} = 43.2 \text{ cm}^2\text{V}^{-1}\text{s}^{-1}$, $V_T = -0.7$ V, $S = 0.2$ V/decade) were fabricated (see Supplementary Fig. S5) and compared with ZnON TFTs. Figure 4a summarizes the transfer characteristics of the TFTs both in the dark and under illumination (15,400 lux). First, it is observed that a-IZO TFTs are highly sensitive to visible light and the device cannot

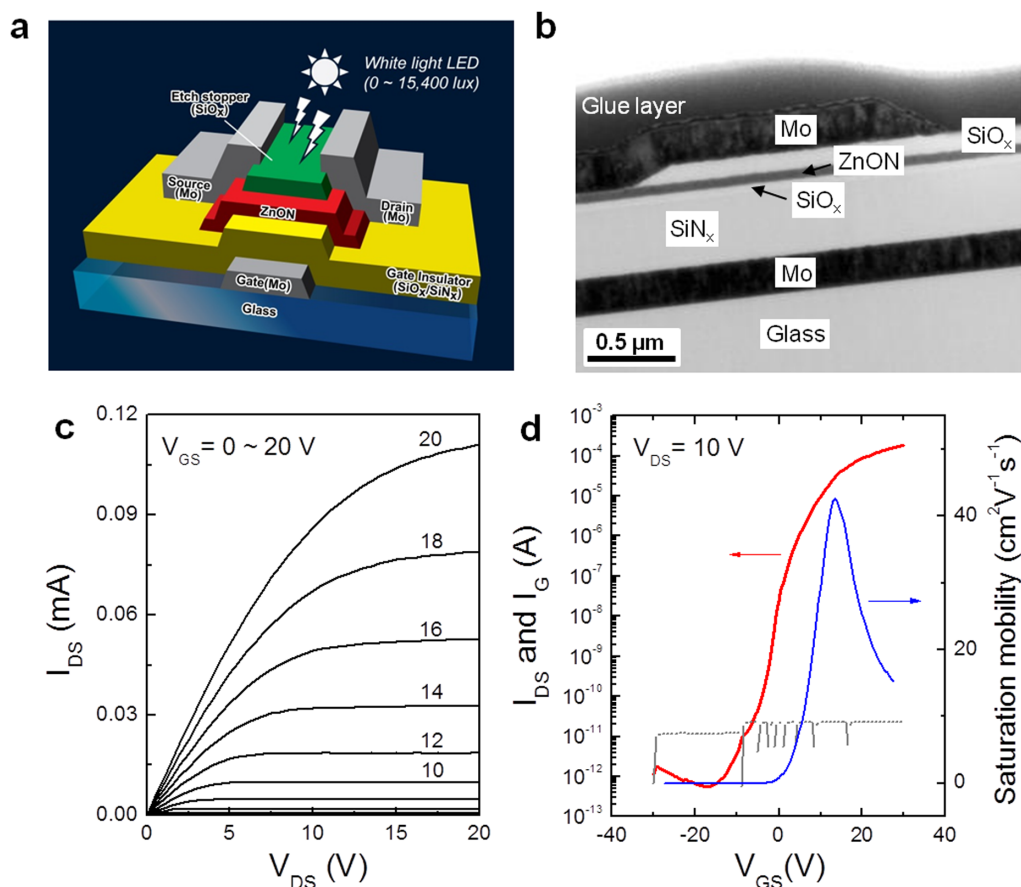


Figure 3 | Typical ZnON TFT characteristics. (a) Schematic of the fabricated ZnON TFT device with an inverted staggered bottom-gate structure. A white-light LED with a tunable luminance of up to 15,400 lux was used in order to supply visible light. SiO_x is a well-known insulator material with a wide band gap of 8.5–9 eV, and transparent or inactive in the visible light range (photon energy, $h\nu = 1.65 \sim 3.18$ eV). Therefore, most of the visible light goes through the etch-stopper layer and reaches the ZnON active layer. (b) Cross-sectional TEM image of the fabricated TFT structure consisting of a glass substrate, Mo gate electrode (200 nm), SiN_x (350 nm)/SiO_x (50 nm) gate insulator, ZnON (50 nm) for the active channel, SiO_x (100 nm) etch-stopper layer, and Mo (200 nm) for the source/drain electrodes. (c) Output (I_{DS} - V_{DS}) curves which were collected at different V_{GS} as marked. (d) Transfer curves (I_{DS} - V_{GS}) acquired with a V_{DS} of 10 V.

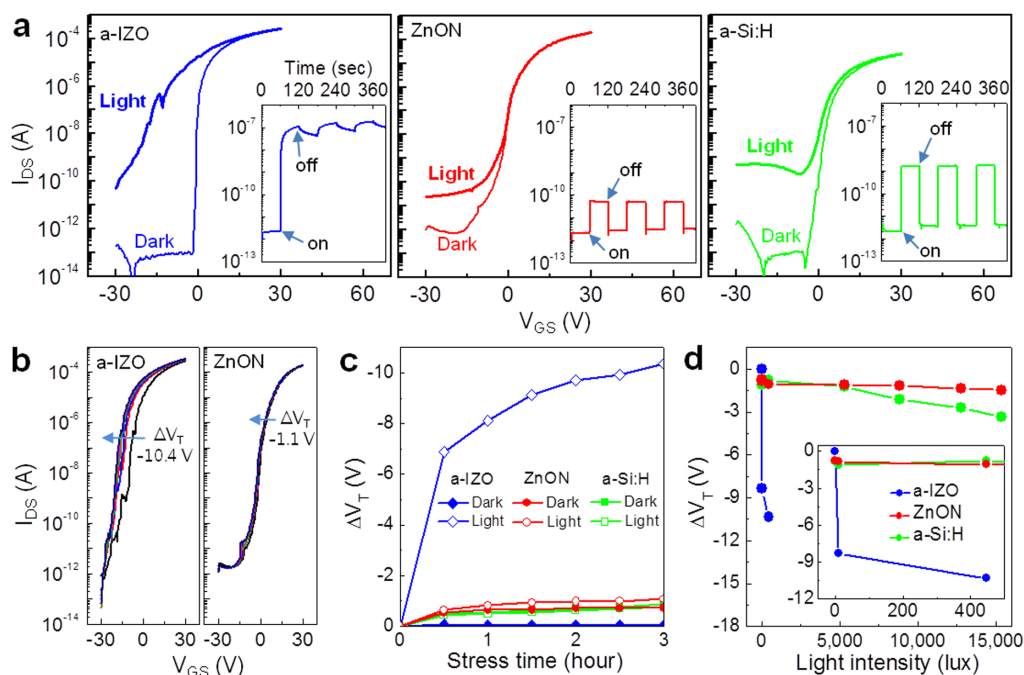


Figure 4 | The photo-stability of ZnON TFTs. Data on a-IZO and a-Si:H TFTs are also shown for comparison. (a) Transfer characteristics of the TFTs both in the dark and under illumination (15,400 lux). Inset shows the source-to-drain current (I_{DS}) as a function of time as the TFTs are subjected to illumination at an intensity of 15,400 lux, turned on and off with a time interval of 60 sec. (b) Parallel negative shifts in the transfer characteristics of the TFTs under illumination (445 lux). (c) Threshold voltage shift (ΔV_T) as a function of stress time under dark and illumination (445 lux). (d) ΔV_T as a function of light intensity illuminating the TFTs. Inset is an enlarged graph showing ΔV_T under weak illumination < 500 lux.

be turned off with the application of gate voltages down to -30 V. Furthermore, the photo-current ($>10^{-7}$ A) increases by more than five orders of magnitude on illumination, and persists long even after the illumination has been turned off (left inset of Fig. 4a), which is related to the NBI instability^{6,9,10,12,13}. On the other hand, ZnON TFTs exhibit inappreciable V_T shift under exposure to visible light and very low photo-currents ($<10^{-10}$ A; ref. 27) with magnitudes smaller than even that of a-Si:H ($\sim 10^{-9}$ A), and do not suffer from the V_T shift via the fast recombination or recovery by band-to-band transition under such a harsh illumination of 15,400 lux (typical office lighting conditions lie between 320–500 lux).

An important performance metric, particularly for the TFTs in FPDs, is the operational device stability under illumination^{2,5,7,8}, i.e., when both light and electrical bias are applied simultaneously. In the dark, IZO TFTs show very stable performance with almost no V_T shift (ΔV_T) as a function of stress time (see Supplementary Fig. S6a), however, a huge negative V_T shift (~ 10 V) occurs even under weak illumination (Fig. 4b; Supplementary Fig. S6a). In contrast, illuminated ZnON TFTs operate stably with no apparent performance degradation (Fig. 4b and 4c; Supplementary Fig. S6c) and the good stability is maintained even at a maximum light intensity of 15,400 lux. Such a level of stability is comparable to that of a-Si:H TFTs (Fig. 4c and 4d; Supplementary Fig. S6b). The superior device stability of ZnON TFTs may originate from the fact that much less photo-excited carriers are generated with a higher recombination rate compared to a-IZO (see Fig. 4a).

Discussion

In the present work, we have demonstrated that the addition of non-oxide anions into oxide semiconductors can offer an effective way to circumvent NBI instability which is the most critical drawback in oxide semiconductors. In particular, we showed the typical example of oxide semiconductor ZnO, where the valence band could be controlled to remove or passivate the V_o levels by substitutional alloying with nitrogen anions. The TFT devices based on ZnON as active

channel layer demonstrate the real suppression of persistent photo-currents under negative bias, and excellent device stability even in the presence of visible light radiation, in contrast to conventional AOSs with similar mobilities exceeding 30 $\text{cm}^2\text{V}^{-1}\text{s}^{-1}$. It is thus anticipated that our approach of controlling anions will open a new avenue to the realization of high-performance and high-stability microelectronics and optoelectronics including displays based on AOS. Additionally, the ability to suppress the adverse V_o effect may shed light on other oxide systems that suffer from V_o .

Methods

All samples were prepared on 15 $\text{cm} \times 15$ cm glass substrates. Prior to film deposition, the substrates were chemically cleaned using aqueous mixtures of H_2SO_4 and H_2O_2 , followed by deionized water rinsing. ZnON films were fabricated by reactive radio-frequency (RF) magnetron sputtering (ULVAC, SME-200U) using a mixture of N_2 , O_2 , and Ar as working gases, where the purity of the sputtering gases was 99.999%. Each gas was introduced through separate mass flow controllers. A sputtering chamber was evacuated to below 2.0×10^{-5} Pa with a turbomolecular pump and a mechanical rotary pump. A 5-inch diameter Zn (purity 99.99%) target was used and the substrates were mounted on a rotating holder at a distance of 18 cm from the target. Prior to deposition, the target was pre-sputtered with Ar ions for 30 min to remove unintentional contaminations on the surface. ZnON films were grown at a substrate temperature of 50°C with a RF sputtering power of 300 W. In order to control the anion contents in the films, the O_2 partial pressure (3.6–28.1 mPa) in the chamber was varied during the deposition by adjusting the O_2 flow rate (1–4 sccm) and the total gas pressure (0.4–0.8 Pa), while the N_2 (100 sccm) and Ar flow rates (10 sccm) were kept constant.

The crystal structures of the films were examined by grazing incidence X-ray diffraction (GIAXRD) analyses using $\text{CuK}\alpha$ radiation (PANalytical, X'pert Pro). The microstructure and crystallinity of the films were observed in detail using transmission electron microscopy (a Cs-corrected FEI Titan operating at 300 kV) and fast Fourier transform (FFT) analysis. AFM images were obtained using a scanning probe microscope (Veeco, Dimension V) in tapping mode with Si probe tips. The film thickness was determined by a surface profilometry (KLA Tencor, P16) to be approximately 50 nm. Optical spectra were acquired with a Cary 5000 ultraviolet-visible-near-infrared spectrophotometer. In order to investigate the bonding state of the films, XPS analysis was carried out using a PHI VersaProbe XPS Microprobe, equipped with an Al X-ray source, K radiation (1486.8 eV) in ultrahigh vacuum, with a pass energy of 23.5 eV (energy resolution better than 0.77 eV as determined on a silver sample). Samples were sputtered for 1 min using Ar ions, which have a sputtering rate of 1.0 nm/min with reference to SiO_2 , in order to remove surface



contaminations. The measured binding energies were referenced to Zn 2p³ peak at 1021.8 eV. For accurate composition analysis of Zn, O, and N in the films, a high-resolution Rutherford backscattering system (KOBELCO, HRBS-V500) equipped with a magnetic sector analyzer capable of obtaining a high-resolution energy spectrum of the Medium Energy Ion Scattering Spectroscopy (MEIS) level was used. The RBS analysis was carried out with a 450 keV He⁺ probe beam, with an incident angle of 50° and a scattering angle of 70.5°. The electrical properties of thin films such as carrier concentration and Hall mobility were measured at room temperature using the four-probe Van der Pauw technique (nanometrics, HL5500).

ZnON TFTs with an inverted staggered bottom-gate and top-contact configuration (Figure 3a) were fabricated on glass substrates (15 cm × 15 cm) using standard semiconductor fabrication process. The integration of TFT devices was done firstly by direct-current (DC) sputter depositing a 200-nm-thick Mo gate at room temperature, and subsequently growing a dielectric stack of a 350-nm-thick SiN_x and a 50-nm-thick SiO₂ at 350°C by plasma-enhanced chemical vapor deposition (PECVD). The ZnON active layer with a thickness of 50 nm was then deposited through a reactive sputtering process as previously described, using a Zn target at a substrate temperature of 50°C. Subsequently, a 100-nm-thick SiO_x etch-stopper layer was deposited at 200°C by PECVD, and then, 200-nm-thick Mo was sputtered at room temperature to form the source-drain electrodes. The deposition conditions for the etch-stopper layer (i.e., SiH₄/N₂O = 10/500 sccm) were optimized to minimize the hydrogen incorporation into ZnON layer. All patterning was done by photolithography and appropriate use of wet or dry etching. The above transistors were then annealed in air for 1 h at 250°C. As references, a-IZO TFTs with the same device structure described above, where the cation ratio (atomic %) for the IZO active layer is In:Zn = 85:15, and a-Si:H TFTs with a back-channel-etch (BCE) structure were also fabricated.

Devices with channel width/length = 50/30 μm for ZnON and a-IZO TFTs and 15/5 μm for a-Si:H TFTs were characterized at room temperature in a vacuum chamber (CryoVac, Vacuum Probe Station) to prevent ambient effects, which can be evacuated to below 1.0 × 10⁻³ Pa with a semiconductor parameter analyzer (Keithley, 4200-SCS). The threshold voltage (V_T), subthreshold swing (S), and saturation field-effect mobility (μ_{sat}) were extracted in compliance with the gradual channel approximation²⁵. The μ_{FE} and V_T were obtained from the transfer curves in the saturation region (V_{DS} = +10 V) using I_{DS} = (C_{ox} · μ_{sat} · W/2L) · (V_{GS} - V_T)², where C_{ox} is the capacitance of the SiO_x(50 nm)/SiN_x(350 nm) gate dielectric stack (C_{ox} = 12.5 nFcm⁻²). The S was taken as the minimum value of the inverse slope of the log₁₀(I_{DS}) versus V_{GS} characteristics. The on-to-off current ratio was calculated from the maximum I_{DS} divided by the minimum I_{DS} in the transfer curve. The amount of hysteresis was defined as the difference between the threshold voltages extracted from the forward and reverse sweeps of the transfer curves. The negative gate bias stress measurements were done at room temperature with simultaneous exposure to visible light. During the stress experiments, a V_{GS} of -20 V and a V_{DS} of +10 V were applied to each TFT device for a total duration of 3 hours. A white-light LED with a tunable luminance of up to 15,400 lux (Sol, LED Light Source) was used in order to supply visible light. During the stress measurements, transfer curves (V_{DS} = +10 V) were collected every 30 min to extract the V_T as a function of stress time. A pristine device was used for each stress measurement. The photo-response against light illumination was also examined from the I_{DS} as a function of time, as the light radiating the TFTs were turned on (15,400 lux) and off with a time interval of 60 sec.

We used Vienna Ab-initio Simulation Package (VASP; ref. 28) to carry out first-principles calculation within density functional theory, employing the projector-augmented wave (PAW) potential for ionic potentials²⁹. The exchange-correlation energy between electrons are described within the hybrid functional developed by Heyd-Scuseria-Ernzerhof (HSE; ref. 30) except for the melt-quench simulation to obtain a-ZnON where the generalized-gradient-approximation (GGA; ref. 31) is used to avoid the sheer computational cost of the hybrid functional. The mixing parameters in the HSE functional were chosen to fit the experimental band gap³², and they are 0.37 (c-ZnO), 0.25 (c-In₂O₃), 0.29 (c-Zn₃N₂), and 0.33 (a-ZnON). The energy cutoff is set to 500 eV for all model systems in the present work. The k-point meshes are chosen on the basis of convergence in the total energy and force within 5 meV/atom and 5 meV/Å, respectively. For a-ZnON, we made amorphous structure using melt-quenching method. Initially, the wurtzite structure of ZnO is used and half of O atoms are replaced with N atoms to mimic our optimized Zn_{56.3}O₂₂N_{21.7} sample. Some O and N atoms are removed from the model system to satisfy the stoichiometry conditions. The supercell consists of 108 atoms; 60 Zn, 24 O and 24 N atoms. The model system was melted at 2000 K for 20 ps, and then it was rapidly quenched to room temperature with the cooling rate of 100 K/ps in order to avoid the formation of N₂ molecule and phase separation into Zn₃N₂ and ZnO.

1. Arai, T. & Sasaoka, T. Emergent oxide TFT technologies for next-generation AM-OLED displays. *2011 SID International Symposium Digest of Technical Papers* **42**, 710–713 (2011).
2. Kamiya, T., Nomura, K. & Hosono, H. Present status of amorphous In-Ga-Zn-O thin-film transistors. *Sci. Technol. Adv. Mater.* **11**, 044305 (2010).
3. Nomura, K. *et al.* Room-temperature fabrication of transparent flexible thin-film transistors using amorphous oxide semiconductors. *Nature* **432**, 488–492 (2004).
4. Nomura, K. *et al.* Thin-film transistor fabricated in single-crystalline transparent oxide semiconductor. *Science* **300**, 1269–1272 (2003).
5. Park, J. S., Maeng, W.-J., Kim, H.-S. & Park, J.-S. Review of recent developments in amorphous oxide semiconductor thin-film transistor devices. *Thin Solid Films* **520**, 1679–1693 (2012).

6. Lany, S. & Zunger, A. Anion vacancies as a source of persistent photoconductivity in II-VI and chalcopyrite semiconductors. *Phys. Rev. B* **72**, 035215 (2005).
7. Kwon, J.-Y. *et al.* Investigation of light-induced bias instability in Hf-In-Zn-O thin film transistors: A Cation combinatorial approach. *J. Electrochem. Soc.* **158**, H433–H437 (2011).
8. Kim, H.-S. *et al.* The influence of In/Zn ratio on the performance and negative-bias instability of Hf-In-Zn-O thin-film transistors under illumination. *IEEE Electron Device Lett.* **32**, 1251–1253 (2011).
9. Ghaffarzadeh, K. *et al.* Persistent photoconductivity in Hf-In-Zn-O thin film transistors. *Appl. Phys. Lett.* **97**, 143510 (2010).
10. Ghaffarzadeh, K. *et al.* Instability in threshold voltage and subthreshold behavior in Hf-In-Zn-O thin film transistors induced by bias-and light-stress. *Appl. Phys. Lett.* **97**, 113504 (2010).
11. Chowdhury, M. D. H., Migliorato, P. & Jang, J. Light induced instabilities in amorphous indium-gallium-zinc-oxide thin-film transistors. *Appl. Phys. Lett.* **97**, 173506 (2010).
12. Jeon, S. *et al.* Gated three-terminal device architecture to eliminate persistent photoconductivity in oxide semiconductor photosensor arrays. *Nature Mater.* **11**, 301–305 (2012).
13. Ahn, S.-E. *et al.* Metal Oxide Thin Film Phototransistor for Remote Touch Interactive Displays. *Adv. Mater.* **24**, 2631–2636 (2012).
14. Jansen, M. & Letschert, H. P. Inorganic yellow-red pigments without toxic metals. *Nature* **404**, 980–982 (2002).
15. Asahi, R., Morikawa, T., Ohwaki, T., Aoki, K. & Taga, Y. Visible-Light Photocatalysis in Nitrogen-Doped Titanium Oxides. *Science* **293**, 269–271 (2001).
16. Khan, S. U. M., Al-Shahry, M. & Ingler Jr, W. B. Efficient Photochemical Water Splitting by a Chemically Modified n-TiO₂. *Science* **297**, 2243–2245 (2002).
17. Umebayashi, T., Yamaki, T., Itoh, H. & Asai, K. Band gap narrowing of titanium dioxide by sulfur doping. *Appl. Phys. Lett.* **81**, 454–456 (2002).
18. Sakthivel, S. & Kisch, H. Daylight Photocatalysis by Carbon-Modified Titanium Dioxide. *Angew. Chem. Int. Ed.* **42**, 4908–4911 (2003).
19. Agoston, P., Albe, K., Nieminen, R. & Puska, M. J. Intrinsic n-Type Behavior in Transparent Conducting Oxides: A Comparative Hybrid-Functional Study of In₂O₃, SnO₂, and ZnO. *Phys. Rev. Lett.* **103**, 245501 (2009).
20. Ye, Y., Lim, R. & White, J. M. High mobility amorphous zinc oxynitride semiconductor material for thin film transistors. *J. Appl. Phys.* **106**, 074512 (2009).
21. Futsuhara, M., Yoshioka, K. & Takai, O. Structural, electrical and optical properties of zinc nitride thin films prepared by reactive rf magnetron sputtering. *Thin Solid Films* **322**, 274–281 (1998).
22. Suda, T. & Kakishita, K. Band-gap energy and electron effective mass of polycrystalline Zn₃N₂. *J. Appl. Phys.* **99**, 076101 (2006).
23. Xing, G. Z. *et al.* Structural and electrical characteristics of high quality (100) oriented-Zn₃N₂ thin films grown by radio-frequency magnetron sputtering. *J. Appl. Phys.* **108**, 083710 (2010).
24. Kang, Y. *et al.* Microscopic origin of universal quasilinear band structures of transparent conducting oxides. *Phys. Rev. Lett.* **108**, 196404 (2012).
25. Sze, S. M. & Ng, K. K. *Physics of Semiconductor Devices* (Wiley, 2007).
26. Long, R., Dai, Y., Yu, L., Huang, B. & Han, S. Atomic geometry and electronic structure of defects in Zn₃N₂. *Thin Solid Films* **516**, 1297–1301 (2008).
27. Ahn, K.-S. *et al.* Enhanced photoelectrochemical responses of ZnO films through Ga and N codoping. *Appl. Phys. Lett.* **91**, 231909 (2007).
28. Kresse, G. & Hafner, J. *Ab initio* molecular dynamics for liquid metals. *Phys. Rev. B* **47**, 558–561 (1993); *Ab initio* molecular-dynamics simulation of the liquid-metal-amorphous-semiconductor transition in germanium. *Phys. Rev. B*, **49**, 14251–14269 (1994).
29. Blöchl, P. E. Projector augmented-wave method. *Phys. Rev. B* **50**, 17953–17979 (1994).
30. Heyd, J., Scuseria, G. E. & Ernzerhof, M. Hybrid functional based on a screened Coulomb potential. *J. Chem. Phys.* **118**, 8207–8215 (2003).
31. Perdew, J. P., Burke, K. & Ernzerhof, M. Generalized gradient approximation made simple. *Phys. Rev. Lett.* **77**, 3865–3868 (1996).
32. Park, S., Lee, B., Jeon, S. H. & Han, S. Hybrid functional study on structural and electronic properties of oxides. *Curr. Appl. Phys.* **11**, S337–S340 (2011).

Acknowledgments

The authors are grateful to SAIT colleagues Y. Kim, Y. K. Cha and C. Y. Moon for assistance with the experiments. This work was supported by the Center for Multiscale Energy System. The computations were carried out at KISTI (KSC-2011-C3-17).

Author contributions

H.-S.K., M.R. and S.Y.L. designed this work. H.-S.K. and S.H. wrote the manuscript. H.-S.K., J.S.P., T.S.K., K.S.S. carried out the experiments and electrical measurements. E.L., J.G.C. and H.L. contributed to TEM, XPS and RBS analysis, respectively. S.H.J. and S.H. performed the DFT calculations. All authors discussed the results and commented on the manuscript. The project was supervised by K.K.



Additional information

Supplementary information accompanies this paper at <http://www.nature.com/scientificreports>

Competing financial interests: The authors declare no competing financial interests.

License: This work is licensed under a Creative Commons Attribution-NonCommercial-NoDerivs 3.0 Unported License. To view a copy of this license, visit <http://creativecommons.org/licenses/by-nc-nd/3.0/>

How to cite this article: Kim, H. *et al.* Anion control as a strategy to achieve high-mobility and high-stability oxide thin-film transistors. *Sci. Rep.* 3, 1459; DOI:10.1038/srep01459 (2013).